



Electrocatalytic Activity of Nitrogen-Enriched Mesoporous Carbon Framework and its Hybrids with Metal Nanoparticles Fabricated through Pyrolysis of Block Copolymers

Journal:	<i>RSC Advances</i>
Manuscript ID	RA-ART-10-2015-022528.R1
Article Type:	Paper
Date Submitted by the Author:	24-Nov-2015
Complete List of Authors:	Lu, Yen-Hsing; National Central University Liou, Jiun-You; National Central University Lin, Chien-Fu; National Central University Sun, Ya-Sen; National Central University, Department of Chemical and Materials Engineering
Subject area & keyword:	Nanomaterials - Nanoscience < Nanoscience

Electrocatalytic Activity of Nitrogen-Enriched Mesoporous Carbon Framework and its Hybrids with Metal Nanoparticles Fabricated through Pyrolysis of Block Copolymers[†]

Yen-Hsing Lu, Jiun-You Liou, Chien-Fu Lin, and Ya-Sen Sun^{a*}

Department of Chemical and Materials Engineering, National Central University, Taoyuan 32001, Taiwan

RSC Advances

Submission: October 2015

Revision: November 2015

* Author to whom correspondence should be addressed:

E-mail: yssun@cc.ncu.edu.tw

Abstract

Nanostructures with a nitrogen-enriched mesoporous carbon framework (NEMCF) were prepared through a simple carbonization of cross-linked polystyrene-block-poly(2-vinylpyridine). NEMCF has a rich mesoporosity because of the morphological fidelity upon cross-linking and carbonization. Hybrids of NEMCF with metal nanoparticles (i.e., Ag@NEMCF) or binary metal alloys (i.e., Ag-Au@NEMCF) were prepared through a photochemical reduction or a photochemical reduction and galvanic replacement in combination. The inner architecture, the chemical composition and the graphitization of NEMCF and MEMCF-supported metal nanomaterials were studied with electron imaging, X-ray and Raman scattering, and electron spectra; the electrocatalytic activity of oxygen reduction in a basic electrolyte was measured with a rotating disk electrode. The nitrogen configurations of NEMCF were dominated by pyridinic and pyrrolic nitrogen, so that NEMCF displayed a two-electron transfer pathway for oxygen reduction reaction (ORR). As Ag NP and Ag-Au alloys composed of minor Au and major Ag were incorporated within the NEMCF matrix, a four-electron transfer pathway, a large kinetic current density and a small onset potential were obtained. Nevertheless, the electrocatalytic activity of the Ag-Au alloys within the NEMCF depended strongly on the compositional proportion, the size of the Au component and the extent of dispersion of Ag-Au alloys.

Introduction

Carbon nanostructures of zero, one, two or three dimensions (0D–3D) have aroused great interest because they show noticeable electrochemical activity due to their unique electrical and chemical properties.¹⁻² In particular, doping carbon nanomaterials with heteroatoms or incorporating metal nanoparticles (NP) into the carbon nanomaterials to tune their electrochemical properties effectively can provide opportunities for the design of diverse new applications with outstanding properties.¹⁻² For instance, nitrogen-doped carbon nanotubes (N-doped CNT),³ graphene sheets (GS)⁴ and graphene quantum dots (GQD)⁵ showed highly effective electrocatalytic activity for the oxygen reduction reaction (ORR). Several methods to fabricate carbon nanomaterials doped with nitrogen atoms have been reported; these methods include the growth of N-doped few-layer GS^{4,6-8} and N-doped CNT via chemical vapor deposition in the presence of nitrogen-containing precursors, and the reduction of graphene oxide (rGO) with a nitrogen plasma⁹ or on thermal annealing in the presence of nitrogen-containing molecules or polymers¹⁰⁻¹¹.

The deposition of metal nanoclusters (NC) or NP on graphene-based nanomaterials also displayed superior electrocatalytic activity and improved the stability of the ORR.^{1-2,12-14} A recent report indicated that exploring noble metals, such as gold (Au), silver (Ag) or alloys of both elements as nanoelectrocatalysts in ORR is of significance in both fundamental research and practical applications despite the tremendous progress in Pt- and Pd-based catalysts with the greatest electrochemical activity for the ORR.² Several facile chemical methods for graphene-supported Ag or Au nanomaterials have been demonstrated.¹⁵⁻¹⁶ The principal step in the synthesis involved the reduction of Ag or Au ion precursors on the surface of graphene oxide (GO).¹³⁻¹⁵ For graphene-supported NC or NP, oxygen functionalities of GO sheets can stabilize the dimension and dispersion of metal

nanomaterials whereas the presence of metal nanomaterials can prevent the π - π stacking of graphene sheets when the oxygen functionalities are removed. Both advantages can yield three-dimensional (3D) nanocomposites with improved stability, catalytic activity and even conductivity.¹⁻²

Despite the tremendous progress in graphene-supported nanoelectrocatalysts, there have been reports of adopting an alternative synthesis of nanostructured carbonaceous materials, such as fullerenes,¹⁷ carbon nanofibers,¹⁸ or nanotube cups.¹⁹ These carbon nanostructures, as carbon scaffolds, can also be decorated with metal catalysts with satisfactory dispersion.^{17, 20} The electrocatalytic properties of such nanomaterial hybrids can be tailored through control of their nanostructures. Here we report the controlled assembly of noble metal NP and alloys supported on a 3D mesoporous carbon network as ORR catalysts fabricated through a pyrolysis of block copolymers (BCP) at low temperature. Such systems are attractive targets, as a self-assembly of block copolymers offers access to nanodomains with tunable dimension and rich morphology through control of the volume fraction and molecular mass or through solvent annealing in solvent vapors with a varied extent of selectivity.²¹⁻²² The utilization of the unique self-assembly features for BCP allows the fabrication of carbon nanostructures with a well defined morphology. Self-assembled BCP nanodomains can act as a sacrificial soft template, onto which small molecules are added as carbon precursors.²³⁻²⁶ Pyrolysis at elevated temperatures led to carbonization of the carbon precursors and complete thermal degradation of the BCP template, producing carbon nanostructures. Carbon nanostructures were fabricated from direct pyrolysis of BCP nanodomains without additive.²⁷⁻³⁵ Upon further stabilizing nanodomains through cross-linking via UV irradiation³¹⁻³³ or cyclization via thermal annealing^{27-30, 34-35}, the morphology of the resultant nanostructure can be retained after pyrolysis.

Another attractive advantage is that, if polymer chains of BCP have functional sites available for binding with metal precursor ions through favorable interactions, metal NP/BCP hybrids can be obtained through chemical or photochemical reduction reactions. Poly(vinylpyridine)-based BCP served as templates for the fabrication of nanoscale dots and wire of metal nanomaterials through interactions between lone electron pairs of pyridine rings and metal ions.³⁶⁻⁴² The dimension, size distribution and spatial order of the metal NP can be controlled by the BCP template to exhibit an impressive electrocatalytic activity or tunable electrical and optical properties.⁴³⁻⁴⁴ For the tests, the BCP nanodomains acted solely in a role of template and were removed by plasma or UV-ozone treatment to demonstrate only the properties of metal nanomaterials.⁴³⁻⁴⁴

A recent report indicated a substantial electrocatalytic performance for block copolymer-templated nitrogen-enriched carbon nanostructures with well defined morphology, prepared on pyrolysis of self-assembled polyacrylonitrile-block-poly(*n*-butylacrylate) copolymer.³⁴⁻³⁵ Kim and coworkers reported that the metal/BCP hybrids could be directly pyrolyzed to grow nanostructured metal/carbon hybrids and that these nanomaterials exhibited superior electrocatalytic activity in oxidation of formic acid and methanol.⁴⁵⁻⁴⁶ As far as we are aware, no attempt has been made to synthesize Ag NP and Ag-Au alloys supported on a BCP-templated nitrogen-enriched mesoporous carbon framework (NEMCF) as ORR catalysts; the exact extent of their electrocatalytic activity in ORR is hence poorly understood. Herein we demonstrate ORR electrocatalytic activity exhibited by NEMCF and NEMCF-supported Ag NP and Ag-Au alloys. NEMCF are obtained through the combination of UV irradiation and pyrolysis of nanophase-separated amphiphilic BCP containing poly(2-vinylpyridine), which serves as a nitrogen-enriched carbon precursor, and polystyrene. NEMCF-supported Ag NP were prepared by the selective binding of

silver complex ions with P2VP rings, reduction to form Ag NP by UV irradiation and pyrolysis. The Au component was introduced on immersion of the Ag/NEMCF hybrids into solutions containing gold ions, according to which galvanic replacement (GR) occurred to form Ag-Au alloys within the NEMCF matrix. Understanding of these phenomena is acquired on examining the correlations between the structural and chemical details of these nanomaterials and their ORR electrocatalytic performance.

Experimental Section

Materials

A diblock copolymer PS-*b*-P2VP having molar masses $M_n=118500$ g/mol (molar masses of the two blocks: $M_n^{PS}=48500$ g/mol and $M_n^{P2VP}=70000$ g/mol; the polydispersity index (M_w/M_n) is 1.13) was purchased from Polymer Source, Inc and used as received. Gold(III) chloride hydrate (HAuCl_4), silver nitrate (AgNO_3), potassium carbonate (K_2CO_3), ammonium hydroxide (NH_4OH), *o*-xylene were obtained from Sigma-Aldrich and used as received.

Fabrication of nitrogen-enriched mesoporous carbon framework (NEMCF) and its hybrids with metal nanoparticles

PS-*b*-P2VP powders were dissolved in *o*-xylene under 2h sonication and then aged at room temperature (ca. 25 °C) for 12 h to yield 2 mass % solutions. PS-*b*-P2VP micellar films of approximately 100 nm were spread on substrates via spin coating (1000 rpm, 60s) from the solutions. After complete removal of solvent vapor, the films were exposed to UV irradiation in nitrogen (UVIN) for 6 h (UV lamp: a germicidal lamp of G20T10 20W light tube, SANKYO DENKI®) to cross-link the micellar nanodomains. With UVIN dosage of 51.84 J/cm² the nanodomains could be completely stabilized. The UVIN-treated films were pyrolyzed at 400 or 430 °C for 1 h in a one-zone diffusion furnace filled with Argon (Ar) gas to obtain NEMCF nanostructures. For NEMCF hybrids incorporated with silver nanoparticles (Ag NPs), UVIN-treated PS-*b*-P2VP films were immersed in 0.1 M AgNO_3 in solutions, which were prepared by adding 34 mg AgNO_3 into a binary mixture of 0.2 mL H_2O and 1.8 mL EtOH and then by adding 60 μL NH_4OH . After 20 min of immersion, the specimens were rinsed by deionized water several times to remove unbinding residual ions. UVIN of 6 h was imposed to the Ag precursors-loaded hybrids to grow Ag NPs

which were generated via a reduction reaction. 400 °C- or 430 °C-thermal pyrolysis was imposed on the Ag/BCP hybrids for 1h to obtain Ag/NEMCF hybrids. For fabrication of NEMCF hybrids loaded with Ag-Au alloyed NPs, the Ag/NEMCF hybrids were immersed in 10_{mM} K-gold solutions, which contained 6.8 mg HAuCl₄, 2mL H₂O, 2mL EtOH and 15.2 mg K₂CO₃, for varied time periods: 0.5, 1, 3 and 12h. In K-gold solutions, the galvanic replacement reaction (GRR) occurred spontaneously via the reaction pathways



After GRR, the specimens were rinsed by deionized water to remove residual ions for material characterization, analysis and electrochemical measurements.

Apparatus and Characterization

A Raman microscope was used to observe the Raman inelastic scattering signals excited by a laser with the wavelength 532 nm and with laser power of 5–30 mW. The Raman data were obtained with a 100× microscope objective for Raman excitation/collection. The acquisition time of each Raman spectral curve was 10 s. Spectral resolution was usually set to 3 cm⁻¹ for this cooled CCD detection system (DV401-BV, ANDOR^{TW}) and the spectrometer fitted with a 1200 groove/mm grating. Average spectra were obtained from at least 3 scans in the wavenumber range of 1050-1900 cm⁻¹. The frequency calibration was set by reference to the 520 cm⁻¹ vibrational band of a silicon wafer. The analysis of chemical components of carbon nanostructures and metal/NEMCF hybrids was performed with a XPS system (VG Scientific ESCALab 250) with a Mg Kα radiation (max: 15 keV) of beam size of 650 ~ 120 μm. Thermogravimetric analysis (TGA) measurements were taken using a

TGA-7 Thermogravimetric Analyzer (PERKIN ELMER). Samples (~ 15 mg powder) were heated from room temperature to 700 °C at 10 °C/min. The morphology and nanostructures of NEMCF and metal/NEMCF specimens were investigated with an atomic force microscopy (AFM, SPA400 Seiko), a high-resolution field-emission scattering electron microscope (HR-FESEM, JEOL JSM-7600F) operated at 10 kV and transmission electron microscopy (TEM, Hitachi H-7100) and electron diffraction (ED) performed at 200 kV. Elemental mapping and energy dispersive spectroscopy were measured with high-resolution TEM (HR-TEM, JEN2100&Hotachi S-4800). The film thickness was determined by Alpha-Step (KLA tencor Alpha-Step IQ) or cross-sectional SEM images. UV-vis absorption of specimens supported on quartz was measured with V-670 UV-visible/NIR spectrophotometer (JASCO Analytical Instruments). Grazing incident small angle x-ray scattering (GISAXS) measurements were performed with a Nano-Viewer (Rigaku) using Cu K α X-rays by a rotating copper-anode generator (Nano-viewer, Rigaku) operated at 1.2 kW in vacuum (40 kV and 30 mA) equipped with confocal max-flux optics at National Central University. X-ray scattering images were collected with a 2D areal detector (Pilatus 100K of 83.8 \times 33.5 mm²). Exposure duration of GISAXS measurement was 30 min for NEMCF specimens and 5 min for Metal/NEMCF hybrids. The condition of incident angle was determined at 0.2°, which is a proper angle to acquire scattering images with high signals-to-noise ratio. The scattering vectors in these GISAXS patterns were calibrated by a sample standard of silver behenate. For NEMCF specimens having an interconnected mesoporous 3D framework buried within the specimens, we further analyzed the GISAXS 1D in-plane profile results to reveal their structural details, including pore surface characteristics, pore shape, size distribution, specific surface area, spatial order and pore-network structure with the Igor Pro using simulated scattering models.⁴⁷⁻⁵⁰

Before pyrolysis, the structure of P2VP nanospheres buried within the PS matrix is analogous to polydisperse spheres of constant P2VP SLD within a matrix of uniform PS SLD. Therefore, the in-plane GISAXS intensity is modeled with

$$I(q_{//}) = (\Delta\rho)^2 V_p P(q_{//}) S(q_{//}) \quad (4)$$

Where $\Delta\rho$ and V_p are the SLD contrast between the P2VP spheres and the PS matrix, $P(q_{//})$ and $S(q_{//})$ are the form factor and structure factor scattering from the P2VP spherical nanodomains buried within the PS matrix.⁴⁸ The Schultz distribution function was introduced into model fittings to yield a polydispersity in the P2VP radius.

After pyrolysis, the carbon spherical nanostructures with an interconnected mesoporous 3D framework are analogous to polydisperse spheres being in contact with the surrounding air. In addition to the scattering contribution of the carbon nanostructures, there is an additional isotropic intensity scattered by the interconnected mesoporous channels defined by the packing of carbon nanostructures. For the irregular mesopores, the scattering intensity decay as a function of $q_{//}$ can be analyzed by a Guinier-Porod empirical model to calculate the size and dimensionality of micropores.⁴⁸ To simplify curve fittings, a hard sphere model or a Gaussian shaped peak was assumed for $S(q_{//})$ since the potential energy function describing the interaction among spherical nanocarbons is unknown. To determine the size and fractal dimension of metal NPs within the metal/NEMCF hybrids, 1D GISAXS in-plan profiles were further analyzed by the Beaucage model⁴⁹. The details of the models were described respectively in the literatures.⁵⁰ The fraction of voids were calculated according to equation (5)

$$R_g = R\varepsilon/3(1-\varepsilon) \quad (5)$$

where R_g is the radius of gyration of voids, R the size of carbon nanostructures and ϵ the fraction of voids.⁵¹ For a gram of the carbon nanostructures with a density 1.8g/cm^{-3} ,⁵² the surface area can be calculated according to R_g , R and ϵ .

Electrochemical measurements:

Cyclic voltammograms (CV), amperometry curves, and linear sweep voltammograms of NEMCF and metal/NEMCF hybrids supported on a glassy carbon disk electrode with a diameter of 5 mm (Pine Research Instrument) were measured with a SP-150 electrochemical potentiostation (BioLogic Science Instrument). The electrocatalytic activity of oxygen reduction reaction for the specimens supported on GC was evaluated using a rotating disk electrode (RDE). Before electrochemical measures, GC electrodes were polished mechanically with a $0.05\ \mu\text{m}$ alumina slurry to obtain a mirror-like surface, rinsed with deionized water, and dried. Then NEMCF precursors were spin-coated as a film directly onto the GC disk electrode and then pyrolyzed without further adding any binders. The preparation of incorporation of metal nanoparticles into the NEMCF matrix supported on the GC disk electrode is the same as described previously. RDE measurements were performed at a scan rate of $10\ \text{mV/s}$ or $100\ \text{mV/s}$ using the catalytic materials-covered GC working electrode in N_2 -saturated or O_2 -saturated $0.1\ \text{M}$ KOH aqueous solution. A platinum wire was used as a counter electrode. Potentials were recorded versus a saturated calomel electrode (SCE) used as a reference electrode.

Results and Discussion

Structural, Chemical Characterizations, and Electrocatalytic Activity of Nitrogen-Enriched Mesoporous Carbon Framework (NEMCF)

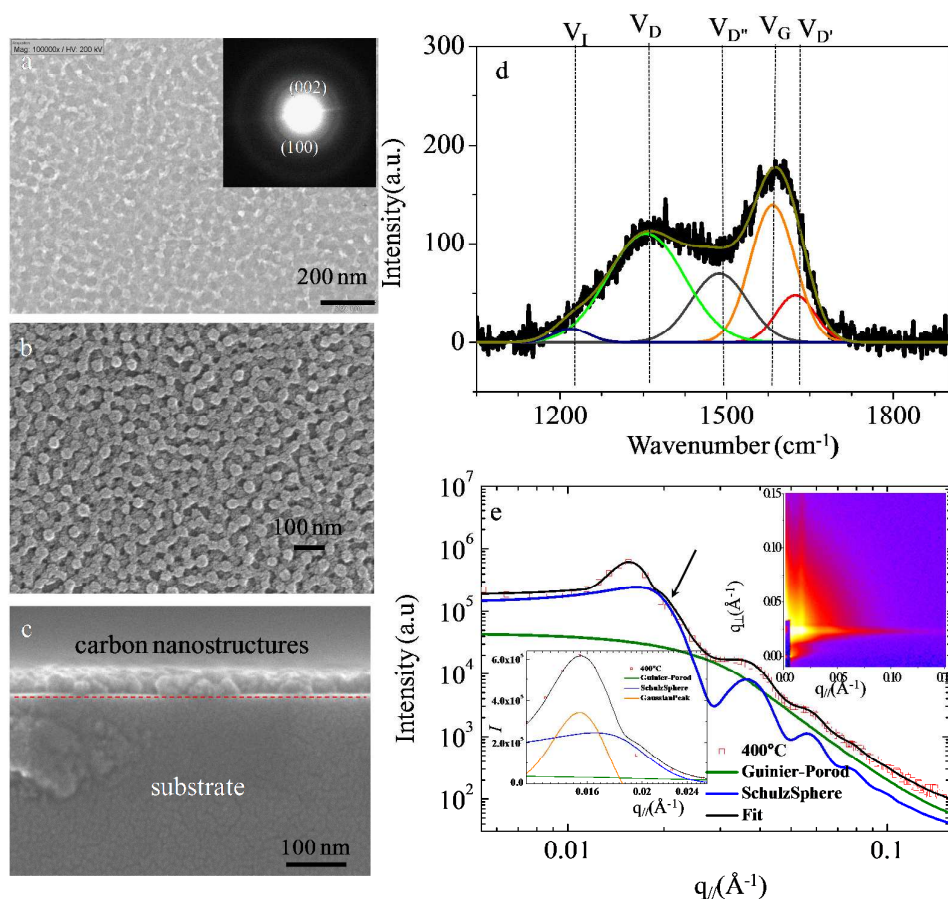


Figure 1 (a) TEM image as well as ED pattern (as an insert) (b) top view and (c) side view SEM images, (d) Raman spectrum, and (e) GISAXS 1D in-plane profile of carbon nanostructures prepared from 400 °C pyrolysis of UVIN-treated PS-*b*-P2VP micelles. The right-top insert of Figure 1 (e) is the corresponding 2D GISAXS pattern while the left-top insert is the Gaussian shaped peak.

NEMCF_y samples were obtained through cross-linking self-assembled spherical micelles of amphiphilic PS-*b*-P2VP BCP with UV irradiation under dinitrogen (UVIN) and subsequent pyrolysis at 400 or 430 °C. Subscript *y* denotes the pyrolysis temperature. The P2VP block played two roles – serving as a nitrogen-enriched carbon precursor and binding with metal ions through favorable interactions due to

lone electron pairs in the plane of the pyridine rings. Images from a transmission electron microscope (TEM) and scanning electron microscope (SEM) clearly revealed an interconnected, porous 3D carbon framework with continuous mesopores in the nanometer range (Figures 1a-c) for NEMCF₄₀₀; the interconnected framework resulted from the packing of carbon nanospheres. As the dimension of the porous channels was controlled by the nano-scale space not occupied by the packing, the interconnected framework with continuous porous channels was in a range a few nanometers. The ED pattern, as shown in the insert, displays two powder rings with d-spacing values 3.33 and 2.02 Å, indexed with (002) and (100) diffraction planes of hexagonal graphite (JCPDS, no 41-4187). This result indicates that NEMCF₄₀₀ is polycrystalline graphite. The Raman spectrum of the resultant NEMCF₄₀₀ shows two broad Raman shifts centered at 1000 and 1900 cm⁻¹ (Figure 1d). The broadening of these two Raman shifts for NEMCF₄₀₀ is ascribed to overlapping of several underlying Raman shifts. A similar feature was discerned for N-doping carbon nanotubes.⁵³ Five components, assigned as I (at 1220 cm⁻¹), D (1487 cm⁻¹), G (1583 cm⁻¹), D' (1624 cm⁻¹) and D'' (1355 cm⁻¹) shifts were used in the fit.⁵⁴⁻⁵⁵ The Raman shift at 1583 cm⁻¹ has been clarified as the graphite mode corresponding to the E_{2g} vibrational mode whereas the Raman shift at 1487 cm⁻¹ is attributed to the formation of disordered species and defects.⁵⁶ Additional characteristic Raman shifts of irregular d₀₀₂ spacing (D' band) and defects (D'') in the layer stacking were recorded for this NEMCF₄₀₀. As the two lines were reported for nitrogen-doped carbons with loss of coherent d₀₀₂,^{53, 57} the observation of the Raman shifts indicates the presence of growing carbon nanostructures with imperfect crystallites. A nanoporous NEMCF₄₀₀ film supported on a silicon substrate was characterized further with grazing-incidence small-angle X-ray scattering (GISAXS) (Figure 1e), of which the inset shows a Bragg truncation rod with uniform isotropic scattering at exit angle $\alpha_i=0.2^\circ$. The truncation

rod is associated with the structural factor of the 3D interconnected framework structure composed of carbon nanospheres, whereas the uniform isotropic scattering is due to the mesopores. A 1D in-plane GISAXS profile with intensity as a function of $q_{||}$ along the $q_{||}$ direction was extracted from the measured 2D GISAXS pattern. The GISAXS 1D profile shows an interference feature at 0.0159\AA^{-1} and fringes in a series for $q_{||} > 0.028\text{\AA}^{-1}$. To obtain quantitative information about structural details such as shape, size, size distribution and surface area of carbon, as well as porous nanostructures, we implemented model simulations with software (Igor).⁴⁷ As Figure 1e shows, the simulated 1D in-plane scan profile show a perfect consistency with the experimental profile. The structural parameters of NEMCF₄₀₀ used in the curve fitting are summarized in Table 1, which shows that the size (R_g) of the mesoporous channels was 6.3 nm and the radius (R) of carbon nanospheres was 15.6 nm. The fraction of voids was calculated as 54% and the total surface area was calculated as $48.3\text{ m}^2/\text{g}$ for NEMCF₄₀₀. The fractal exponent of $D_f=3.77$ indicates that the interface between the voids and interconnected carbon framework is smooth and sharp.⁴⁸

Table 1: Results of fitting the GISAXS in-plane profile for granular carbon nanostructures fabricated from 400 °C-pyrolysis of the PS-*b*-P2VP film.

Parameters used for the Guinier-Porod model	
Rg [nm]	6.3
Porod Exponent	3.77
Parameters used for polydispersive spheres	
mean radius (nm)	15.6
polydispersity	0.09
carbon sphere SLD (\AA^{-2})	5.12×10^{-5}
pore SLD (\AA^{-2})	1.10×10^{-8}
Parameters used for the Guassian shaped peak	
peak center (\AA^{-1})	0.01559
peak width at half maximum	0.00351

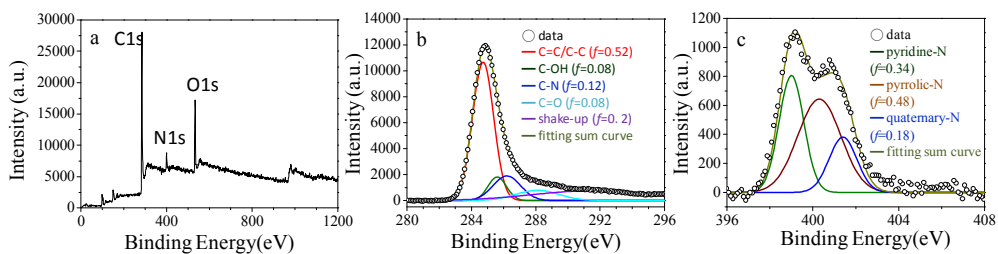


Figure 2 (a) XPS survey spectrum, (b) C_{1s} spectrum and (c) N_{1s} spectrum of $NEMCF_{400}$. The fraction of each component for carbon- and nitrogen-containing species is designated in the figure.

To probe the chemical composition and content of nitrogen in $NEMCF_{400}$, we recorded X-ray photoelectron spectra (XPS) of $NEMCF_{400}$ (Figures 2). In Figure 2a, the survey spectrum of $NEMCF_{400}$ reveals the presence of C, O and N. The ratio of carbon to nitrogen atoms was $\sim 9:1$, indicating a rich nitrogen content for $NEMCF_{400}$.

The XPS C_{1s} of NEMCF shows signals corresponding to carbon species with varied chemical states between 280 and 295 eV, in addition to C=C at 284.7 eV (see Figure 2b). Signals at 285.6, 286.2 and 288.1 eV are assigned to the C_{1s} excitation of the C–OH, C–N, C=O group; one signal at 291.5 eV is attributed to the $\pi \rightarrow \pi^*$ shake-up satellite of aromatic rings.⁵⁸⁻⁶⁰ Figure 2c shows the XPS N_{1s} of NEMCF₄₀₀ resulting from three nitrogen-containing species assigned to pyridinic nitrogen (N6, at 398.4 eV), pyrrolic nitrogen (N5 400.1 eV) and quaternary nitrogen (NQ 401 eV).⁶¹⁻⁶² NEMCF₄₀₀ contained more pyridinic and pyrrolic nitrogen and less graphitic nitrogen. For NEMCF₄₃₀, the nanostructures are similar to NEMCF₄₀₀. Pyrolysis at 430 °C led to only a slightly increased ratio of C to N (~10:1) in NEMCF₄₃₀ (Figure S1). NEMCF₄₃₀ contained more NQ and less N₅ than NEMCF₄₀₀, indicating that pyrolysis at higher temperatures favors the formation of NQ (Figure S1).

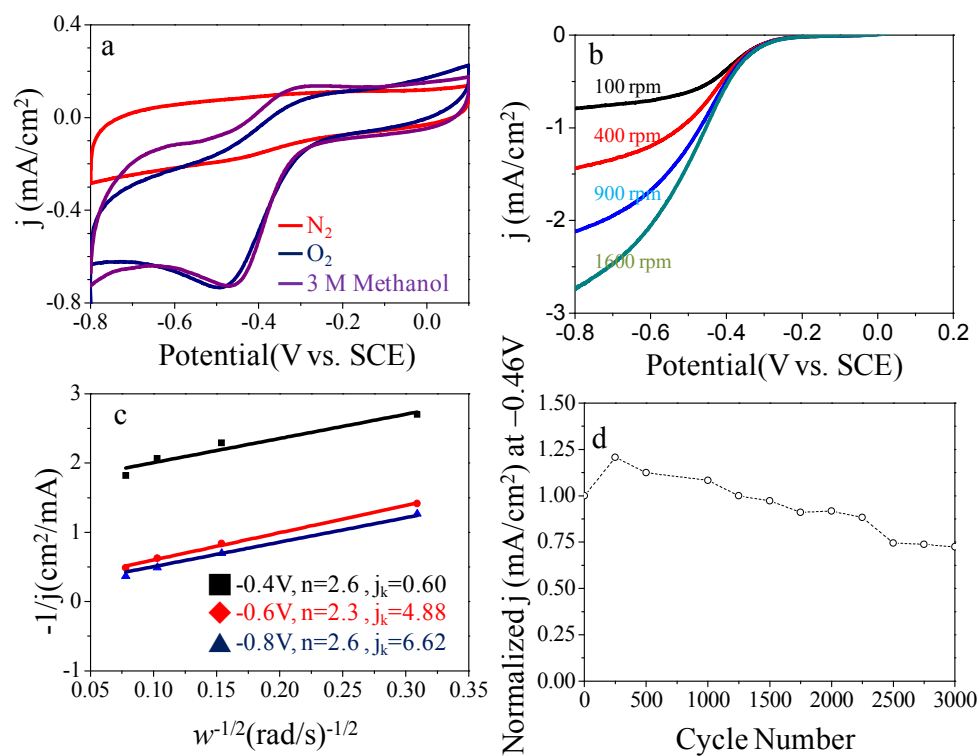


Figure 3 (a) cyclic voltammogram of NEMCF₄₃₀ at a scan rate of 100 mV cm⁻¹ in N₂- or O₂-saturated 0.1 M KOH solutions as well as O₂-saturated 0.1 M KOH solution with 3 M CH₃OH. (b) RDE voltammograms recorded for NEMCF₄₃₀ supported on a GC electrode in an O₂-saturated 0.1 M KOH solution at a scan rate of 10 mV s⁻¹ and different rotation rates; (c) K-L plots of j^{-1} vs $w^{-1/2}$ at -0.4, -0.6 and -0.8 V obtained from (b). (d) Current-cycle chronoamperometric responses at -0.46 V.

The electrocatalytic activity of NEMCF for the ORR was characterized first with cyclic voltammetry at scan rate 100 mV s⁻¹ in a nitrogen-protected or oxygen-saturated KOH solution (0.1 M) (see Figure 3 and Figure S2). Figure 3a shows featureless voltammetric currents within the potential range -0.8 to +0.1 V present for NEMCF₄₃₀ in the N₂-saturated solution. In contrast, a cathodic peak with onset overpotential at -0.235 V (vs. SCE) is discernible, indicative of the electrocatalytic activity of NEMCF. No noticeable crossing effect in NEMCF against the electrooxidation of methanol in O₂-saturated KOH (0.1 M) in the presence of methanol (3 M) indicated a great selectivity and effective stability of NEMCF for the ORR.

To investigate the reaction kinetics for the electrodes, we undertook linear-sweep voltammograms (LSV) with a rotating-disk electrode (RDE) at scan rate 10 mV s⁻¹ and at a rate of rotation from 100 to 1600 rpm in an O₂-saturated KOH electrolyte (0.1 M). The kinetic parameters of ORR, including current density (j), kinetic current density (j_k) and reciprocal of the square root of rotation speed (w), were analyzed on the basis of Koutecky-Levich plots (K-L plots, see supporting information)⁶³

The K-L plots of j^{-1} vs $w^{-1/2}$ at potentials -0.4, -0.6 and -0.8 V on the NEMCF₄₃₀ electrode exhibited satisfactory linearity. Electron transfer numbers calculated from the slope of K-L plots indicated 2.5 as the electron transfer number in NEMCF₄₃₀. Relative to NEMCF₄₃₀, NEMCF₄₀₀, which contains more N5 and N6 and less NQ, shows worse ORR properties (Figure S2). The electrocatalytic performance of

N-doped catalysts was demonstrated to depend on nitrogen bonding configurations, i.e., pyridinic, graphitic and pyrrolic.^{3, 5, 10, 64-75} Interpretation of relations between the nitrogen bond configurations and the ORR performance was difficult and lacked a clear conclusion, but several recent authors studying N-doped graphene and carbon nanostructures have suggested that the carbon atom neighboring NQ exhibits the most active ORR catalytic site, with that in the vicinity of N6 next, and N5 least effective. NQ exhibits a small HOMO-LUMO energy gap and large charge and spin densities, which delivers more positive charges to neighboring carbon atoms, thus serving as active sites with a four-electron reduction path for ORR.⁷²⁻⁷³ Although lone electron pairs at N6 might induce a small polarity of its neighboring carbon atoms and interfere with the adsorption of intermediate HO_2^- species of oxygen reduction at the neighboring carbon atoms, the HO_2^- species might exhibit a strong tendency to desorb into the solution and to decompose directly into O_2 and OH^- species, thus producing a two-electron reduction path in ORR. Such a reduction path was observed for graphene doped with nitrogen atoms containing N6 in major proportions.^{71, 75} This explanation also accounts for the ORR catalytic performance observed for NEMCF₄₃₀ with major proportions of both N5 and N6, and with minor proportion of NQ. We examined the catalytic stability of NEMCF₄₃₀ electrodes toward ORR by measuring the current-cycle chronoamperometric response in O_2 -saturated KOH (0.1 M). In Figure 2d, the current density of NEMCF₄₃₀ retained 72 % of its original electrochemical activity after 3000 cycles of CV scans from -0.8 to $+0.1$ V.

Structural, Chemical Characterizations, and Electrocatalytic Activity of Metal NPs and Alloys Supported within NEMCF

In this section, we demonstrate the efficient electrocatalytic activity exhibited by metal nanoparticles (Ag NP or Ag-Au core-shell NP) supported on NEMCF. To

prepare NEMCF hybrids incorporated with sufficient Ag NP, we modified silver ions with ammonia added to aqueous solution, according to which diamminesilver complex ions (0.1 M) in aqueous solution were obtained. These complex ions have two functionalities: (i) the ammonia ligands can act as a source of nitrogen during pyrolysis, and (ii) the addition of ammonia can preserve charge neutrality of the P2VP block. Yap *et al.* demonstrated that, in aqueous media at acidic pH, the P2VP block exhibits a net positive charge through the protonation of pyridine rings.⁷⁶ For AgNO_3 (0.1 M) in aqueous and ethanol solutions, the solutions exhibit an acidic medium. As a result, positively charged P2VP cannot effectively associate with Ag^+ ions because of electrostatic repulsion, resulting in Ag NP with a small yield (see Figure S3a). In contrast, in the presence of ammonia the positively charged P2VP block might be inhibited so that associating with $\text{Ag}(\text{NH}_3)_2^+$ complex ions within the P2VP block works well even at concentration 0.1 M , making BCP-guided arrays of silver NP possible at a large density (see Figure S3b).

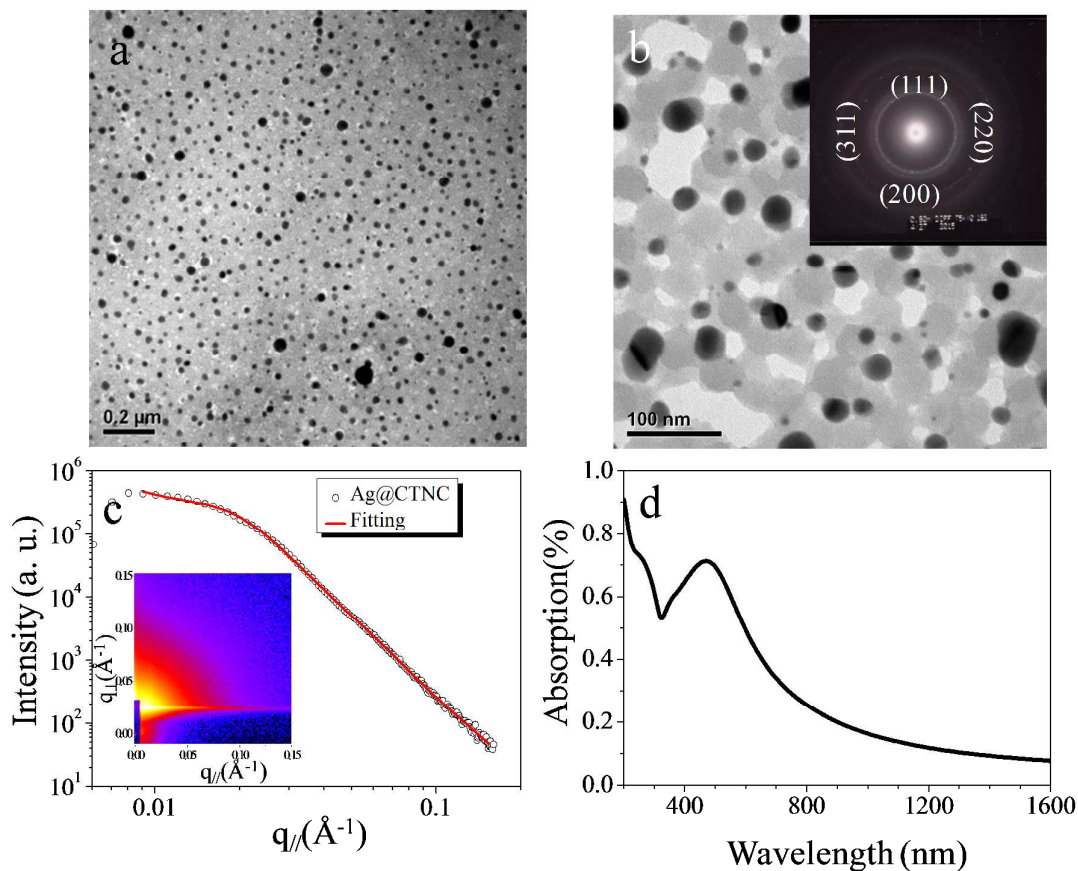


Figure 4 (a) low- and (b) high-magnification TEM images, (c) GISAXS 2D pattern and 1D in-plane profile, (d) UV-vis spectra of Ag@NEMCF₄₀₀. The ED pattern, as shown as insert in (b) shows powder rings which can be indexed as (111), (200), (220) and (311) reflection according to the cubic structure of Ag (JCPDS No. 87-0720).

The optimum temperature of pyrolysis for making metal/NEMCF hybrids was 400 °C not 430 °C as the incorporation of Ag NP decreased the thermal stability of the NEMCF matrix, to be discussed later. After cross-linking of the polymeric templates, reduction of the metal ions with UVIN and pyrolysis, the structure and morphology of Ag@NEMCF₄₀₀ hybrids as prepared were characterized first with a transmission electron microscope (TEM) and grazing incident X-ray scattering or diffraction. The TEM image reveals that silver NP are well embedded within the carbon matrix and the Ag@NEMCF₄₀₀ hybrids show an interconnected mesoporous framework of carbon nanostructures with uniform deposition of Ag NP (Figure 4a, b). The pattern of

electron diffraction indicates the formation of Ag NP in the hybrids (see the inset of Figure 4b). Most silver NP are preferentially located in mesoporous channels rather than within the interconnected carbonaceous framework after pyrolysis. This phenomenon indicates a weak adhesive interaction between Ag NP and the N-enriched carbon. As the cohesive energy of metals is much greater than the adhesive energy between metals and N-enriched carbons, pyrolysis inevitably caused separation of the two phases, but at pyrolysis temperature 400 °C the confined growth of Ag NP was present within the mesoporous channel defined by the packing of spherical nanostructures. In contrast, after pyrolysis at 430 °C, the Ag/NEMCF hybrid revealed a chaotic morphology (see Figure S4). For pyrolysis at 430 °C, the size of Ag NP increased to hundreds of nanometers, much larger than the dimension of the mesoporous channel. This phenomenon indicates that the effect of confinement of the porous carbon matrix on the growth of Ag NP became completely invalid when pyrolysis was conducted at 430 °C. Coalescence between Ag NP without a constrained space produced a sub-micrometer size.

We return to discuss the size and size distribution of Ag NP within the NEMCF₄₀₀ matrix obtained from pyrolysis at 400 °C. As the shape of the silver NP was irregular rather than spherical and as the size distribution was polydisperse, determining the size and size distribution of Ag NP with acceptable statistics from the 2D TEM images was unfeasible. GISAXS and curve fitting were thus implemented to acquire insight into the structural information of Ag NP. The GISAXS 2D pattern shows an isotropic scattering (Figure 4c). For comparison with NEMCF₄₀₀ (Figure 1e), no scattering feature associated with the structural information of carbon nanostructures was present for Ag@NEMCF₄₀₀. This result indicates that the spatial order of carbon nanostructures was destroyed by Ag NP, because the incorporation of Ag NP into the self-assembled nanodomains of PS-b-P2VP BCP decreased the

thermal stability of the carbon nanostructure (see Figure S5). In contrast, Ag NP can grow through limited coalescence within the mesoporous channels during thermal pyrolysis at 400 °C. As the NP growth advanced over the mesoporous space imposed by the packing of carbon nanostructures, the inner structure of NEMCF₄₀₀ would be influenced by the NP growth. Figure 4d shows a GISAXS 1D in-plane profile extracted via a horizontal scan cut from the isotropic scattering of the 2D GISAXS pattern. The 1D GISAXS profile shows that the scattering intensity decays exponentially with $q_{||}$ at small $q_{||}$ and subsequently as a function of $q_{||}$ with power -4 at moderate and large $q_{||}$. The fourth-power decay at moderate and large q indicates the formation of compact Ag NP with smooth and sharp interfaces. Taking the TEM results into account, we analyzed quantitatively the 1D GISAXS profile using the Beaucage model to calculate the radius of gyration (R_g) and the fractal dimension of Ag NP. To fit the curves, we neglected the scattered intensities contributed from NEMCF if they existed; all scattered intensity was from Ag NP. Such an assumption was made for two reasons: Ag NP have a much greater scattering length density than NEMCF, and the original morphology of NEMCF was destroyed by Ag NP. The best fit was obtained with a model comprising two size distributions of NP, which contribute to the scattered intensity to varied extents. The calculated R_g values were 3.9 and 18.2 nm (see Table 2). The small NP are due to UV irradiation-induced primary nanoparticles whereas the large NP are attributed to the coalescence of the primary particles within the mesoporous channels during pyrolysis at 400 °C.

The UV-visible absorption spectrum of the resultant Ag@NEMCF₄₀₀ shows an absorption centered at 466 nm that is attributed to a surface plasmon resonance (SPR) of Ag nanoparticles as shown in Figure 4d. An absorption band centered at ca. 266 nm corresponds to the $\pi \rightarrow \pi^*$ transitions of extended aromatic C-C bonds. The presence of this absorption reflects electronic conjugation within the carbon nanostructures.⁷⁷

The survey spectrum of Ag@NEMCF₄₀₀ reveals the presence of C, O, N and Ag (Figure 5a). Additional evidence for the formation of Ag nanoparticles within the NEMCF₄₀₀ matrix is provided by XPS of the Ag_{3d} core levels; as shown in Figure 5b, the position of the Ag_{3d} lines corresponds to the metallic component. This result indicates that Ag NPs were fabricated from UV-irradiated reduction of ammonia silver complex ions.

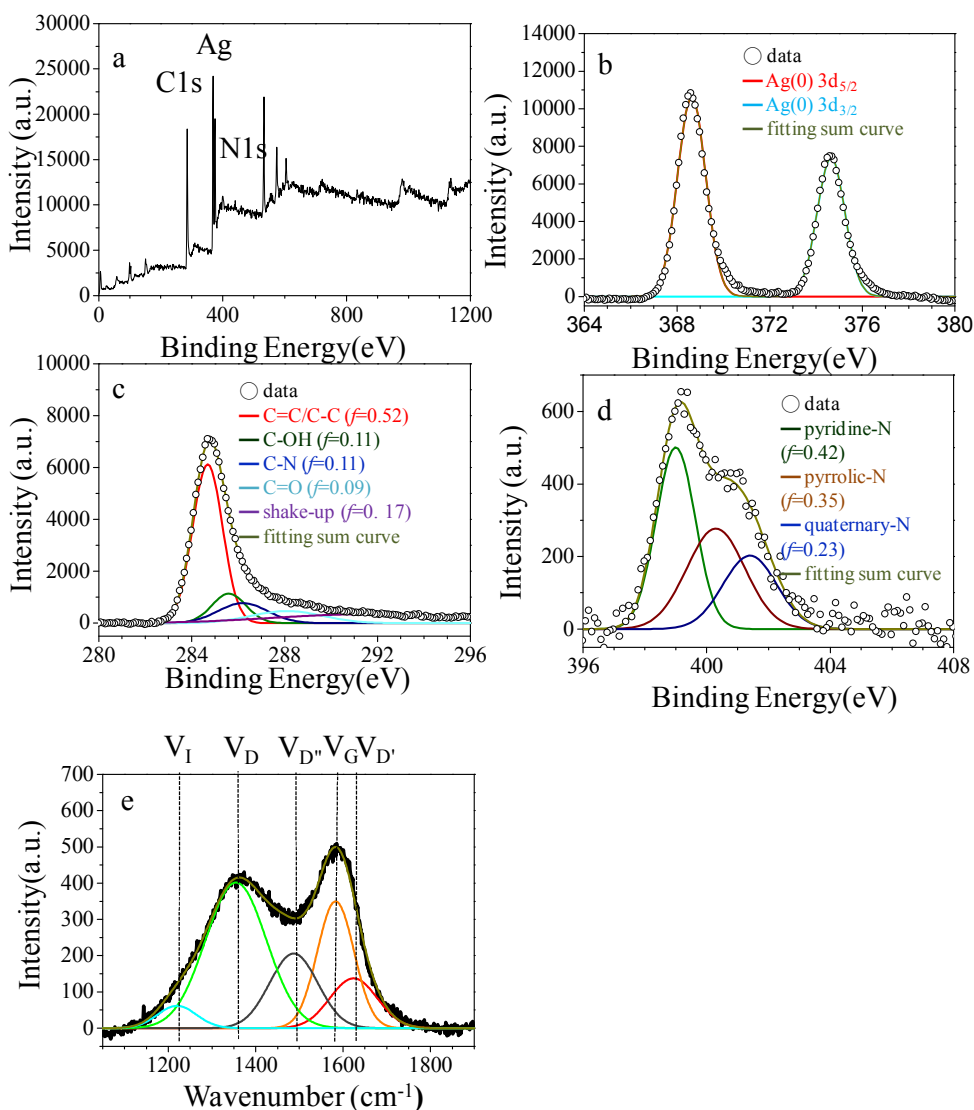


Figure 5 (a) XPS survey, (b) Ag_{3d}, (c) C_{1s} and (d) N_{1s} spectra, and (e) Raman spectrum of Ag@NEMCF₄₀₀.

The ratio of carbon to nitrogen atoms maintained $\sim 10:1$, indicating that the incorporation of Ag NP insignificantly influenced the content of nitrogen atoms. In Ag@NEMCF₄₀₀, Ag was more prevalent than carbon and nitrogen atoms, indicating that the major component consists of Ag NP. That there was no shift of the binding energies of C_{1s} and N_{1s} (see Figure 5c, 5d) demonstrates that Ag@NEMCF₄₀₀ is not a covalent hybrid. Such non-covalent hybridization accounts for the migration and fusion of Ag NP within the NEMCF₄₀₀ matrix during pyrolysis. Ag@NEMCF₄₀₀ has more NQ but less N5 than neat NEMCF₄₀₀, indicating that the presence of Ag NP can improve the extent of graphitization and depress the formation of N5. In the Raman spectrum of Ag@NEMCF₄₀₀, enhanced broad Raman shifts in the range 1000 -- 1900 cm⁻¹ are discerned (Figure 5e). The enhancement of the Raman intensity reflects an enhanced local electromagnetic field resulting from the surface plasmons of silver NP excited with the incident light. As a result, on the surface of Ag NP the cross section of Raman scattering can significantly increase. The contribution to the electromagnetic enhancement is proportional to the magnitude of the electromagnetic fields, which depends on the distance between metal NP and molecules.⁷⁸ Quantitative analysis of the Raman spectrum of Ag@NEMCF₄₀₀ through deconvolution indicates that the enhancement of the D and D' lines associated with disordered defects is great, indicating the preferential location of Ag NP at the defect sites of NEMCF₄₀₀.

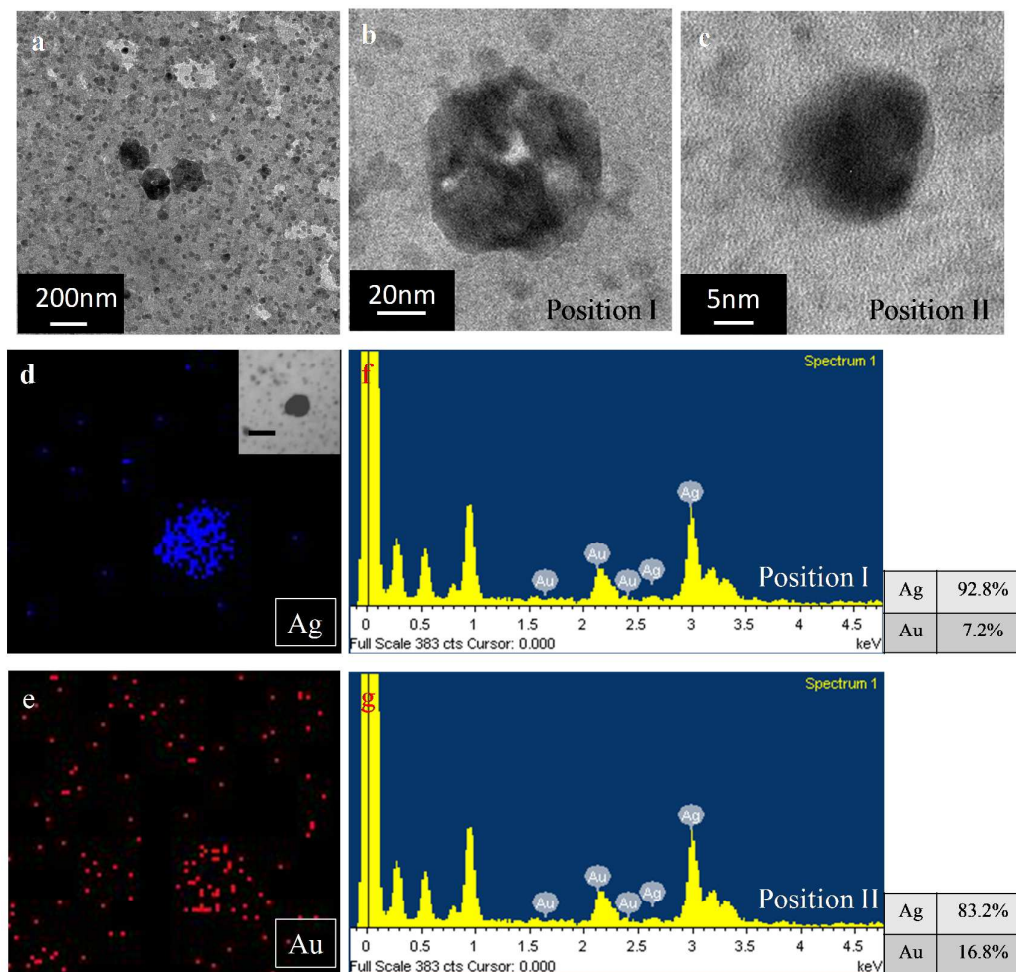


Figure 6 (a-c) typical TEM images, (d-e) elemental mapping and (f-g) EDS patterns of Ag-Au₁@NEMCF₄₀₀. The EDS patterns were collected at positions I and II, which correspond to samples (b) and (c), respectively. The corresponding SEM image for elemental mapping is shown as an insert in Figure 6d.

To prepare Ag-Au core-shell NP supported on three-dimensional NEMCF₄₀₀, we immersed Ag@NEMCF₄₀₀ hybrids into aqueous solutions containing both K₂CO₃ and HAuCl₄ (K-gold solution) for various periods, in which Au clusters or NP grew through GRR at the expense of Ag NP.⁷⁹⁻⁸⁶ After GRR of these varied periods, NEMCF₄₀₀ hybrids with varied Au and Ag content are denoted as Ag-Au_x@NEMCF₄₀₀ (in which *x* implies the duration of reaction, equal to 0.5, 1, 3, and 12 h). We implemented TEM characterization to identify the dispersion of

Ag-Au₁ and Ag-Au₁₂ NP within the carbon matrix. For Ag-Au₁@NEMCF₄₀₀, most Ag-Au NP were uniformly dispersed within the NEMCF₄₀₀ matrix (Figure 6a), but we observed occasionally a few NP of large size, which grew via fusion of small NP preferentially at the surface of the specimen (see Figure 6a, b). We implemented elemental mapping analysis for a selective distribution of the chemical composition of Ag-Au₁@ NEMCF₄₀₀ (Figure 6c, d). That analysis of Ag-Au₁@NEMCF₄₀₀ demonstrated that the outer region of each NP was preferentially dominated by a thin, incomplete alloy shell Au whereas Ag was dominant in the inner region. The atomic ratio of Ag to Au quantitatively determined from energy-dispersive spectra (EDS) was ~13:1 for large NP and ~ 4.95:1 for small NP (see Figure 6f, g), indicating that for Ag-Au₁@NEMCF₄₀₀ Ag is a major component and Au is minor regardless of the particle size. The optical signature of Ag-Au₁@NEMCF₄₀₀ was further studied. For Ag-Au₁@ NEMCF₄₀₀, the resonance signal was slightly blue-shifted and had depressed intensity relative to Ag@NEMCF₄₀₀ (see Figure S6). No near-infrared (NIR) plasmon resonance associated with formation of hollow gold nanoshells was present in the UV-visible data.

GRR of silver NP in an aqueous HAuCl₄ solution is accepted to have a two-step structural evolution. The first step grows hollow nanoshells comprised of Au/Ag alloys through the Kirkendall effect because Ag rapidly diffuses into Au.⁷⁹⁻⁸⁶ The second step brings fragmentation of the hollow nanoshells through dealloying. Each step leads to distinct plasmon resonances, which correlate with structural and compositional evolution. Hollow nanostructures display a red-shifted plasmon resonance in a NIR regime whereas the plasmon resonance is blue-shifted at the stage of fragmentation of the hollow nanostructures into small pieces.⁷⁹⁻⁸⁶ Goodman *et al.* provided a clear interpretation of correlations between plasmon resonances and evolution of the structural composition during NP growth in a GRR;⁷⁹ they found also

that the optical signature of an Ag/Au core-shell structure with pinholes within the Au shell was near that of neat Ag NP. According to their theoretical modeling calculated based on a finite-element method,⁷⁹ we ascribed the blue-shift plasmon resonance at 460.5 nm with depressed intensity to the formation of Ag-Au core-shell NP with surface defects. This result implies that NEMCF₄₀₀ might impose a barrier to diffusion of metal ions. The diffusion of Ag and gold ions might thus be significantly retarded, because, in the presence of NEMCF₄₀₀ with a mesoporous framework structure, Au ions diffuse more slowly from an aqueous medium onto the surface of the Ag NP for GRR to proceed. Ag ions generated through oxidation by Au concurrently become sluggish under the mesoscale confinement, further inhibiting the formation of porous cores. Both factors hence account for the growth of Ag-Au core-shell alloys containing defects on the particle surface. Our control experiment revealed that, without encapsulating of NEMCF, GRR of silver NP in the K-gold solution grew hollow nanostructures with a NIR plasmon resonance at an early GRR stage (Figure S7). Upon prolonged GRR for NEMCF-free Ag NP, there was an accompanying blue shift of the plasmon resonance, indicative of fragmentation of the hollow nanostructures (see Figure S7).

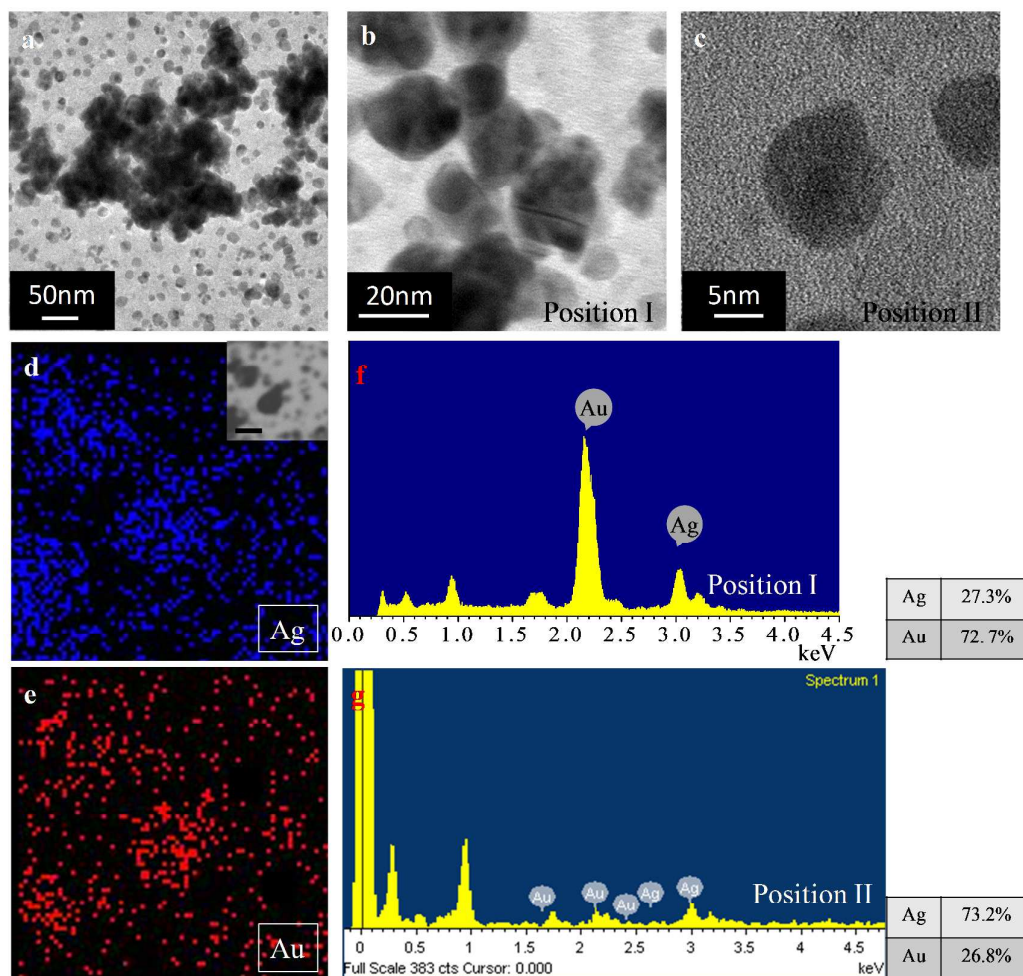


Figure 7 (a-c) typical TEM images, (d-e) elemental mapping and (f-g) EDS patterns of Ag-Au₁₂@NEMCF₄₀₀. The EDS patterns were collected at positions I and II, which correspond to samples (b) and (c), respectively. The corresponding SEM image for elemental mapping is shown as an insert in Figure 7d.

Figures 7a-c show TEM images of Ag-Au₁₂@NEMCF₄₀₀. Prolonged immersion (12 h) of the Ag@NEMCF₄₀₀ hybrid in the K-gold evidently led to aggregation of Ag-Au core-shell NP whereas part of the Ag-Au₁₂ alloys was still well dispersed within the NEMCF₄₀₀ matrix. The aggregates were preferentially located at the free surface of the specimen (Figure S8). For Ag-Au₁₂ alloys within the aggregates, inter-NP fusion and growth were discernible (Figure 7b), indicating that prolonged immersion caused the detachment of metallic NP, beginning from the free surface of

the specimen. As there was no capping layer on the surface of the detached NP for stable dispersion in a liquid medium, aggregation occurred. In contrast the dispersed Ag-Au₁₂ NP within the NEMCF₄₀₀ matrix retained a small size and the interior of each dispersed NP was not oxidized to form a void. Elemental mapping analysis of Ag-Au₁₂@NEMCF₄₀₀ demonstrated that the content of Au was comparable with that of Ag, indicating that Ag NP were increasingly oxidized by Au ions (Figure 7c). EDS characterization and analysis were selectively imposed on the locations of aggregated NP and dispersed NP. As Figures 7 f and g show, the ratio Ag/Au decreased substantially to 0.38:1 for the aggregated NP whereas the ratio Ag/Au decreased slightly to 2.73:1 for the dispersed NP. This result indicates that the growth of Au through GRR is more rapid for the aggregated NP than for the dispersed NP, because, once detached from the NEMCF₄₀₀ matrix onto the free surface, the NP were easily oxidized rapidly by Au ions because of lack of confinement. Without that confinement imparted by NEMCF₄₀₀, the detached NP exhibited a strong tendency to grow further via Oswald ripening or inter-NP coalescence.

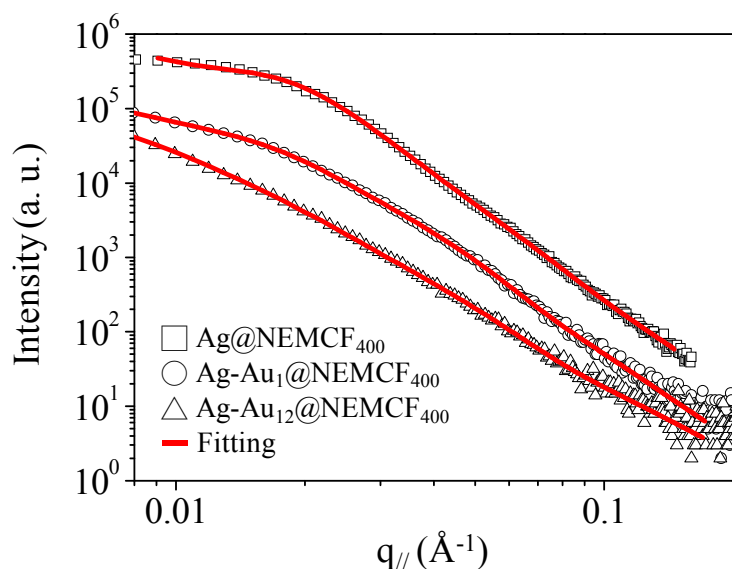


Figure 8 GISAXS in-plane 1D profiles with intensity as a function of $q_{//}$ for

Ag@NEMCF₄₀₀, Ag-Au₁@NEMCF₄₀₀ and Ag-Au₁₂@NEMCF₄₀₀

Table 2 Results of Data Fitting of the Metal NPs and Ag-Au Binary Alloys Incorporated within NEMCF₄₀₀ with the Beaucage Model

metal/carbon hybrids	R_g^1 (nm)	D_f^1	R_g^2 (nm)	D_f^2
Ag@NEMCF ₄₀₀	18.1	4.00	3.9	4.00
Ag-Au ₁ @NEMCF ₄₀₀	19.9	3.53	5.3	3.78
Ag-Au ₁₂ @NEMCF ₄₀₀	23.9	3.29	4.8	3.14

The structural details of Ag-Au₁@NEMCF₄₀₀ and Ag-Au₁₂@NEMCF₄₀₀ were studied also with GISAXS. The results are presented in Figure 8, in which a datum on the incorporation of Ag NP within NEMCF₄₀₀ is included for comparisons. Like Ag@NEMCF₄₀₀, the intensity falls exponentially according to the Guinier approximation in the small- $q_{//}$ region for both Ag-Au₁@NEMCF₄₀₀ and Ag-Au₁₂@NEMCF₄₀₀. As the scattering feature is governed by the particles of size within the Guinier range, the dimension of the aggregates could not be determined with SAXS; only the size of small dispersed Ag-Au primary NP within the matrix and large Ag-Au primary NP within the aggregate could be known through curve fitting based on the empirical Beaucage model.⁵⁰ The curve-fitted structural parameters, as shown in Table 2, show that the radius of gyration for the Ag-Au NP seems to increase with increasing Au component. The small fractal exponent values given by the power-law intensity decay ($I \sim q^{-D_f}$) indicate that prolonged GRR gave a looser structure with a rough surface for the Ag-Au alloys relative to the Ag NP. The large loose structure is due to the non-uniform growth of tiny Au NC or NP on the surface of Ag NP through GRR.

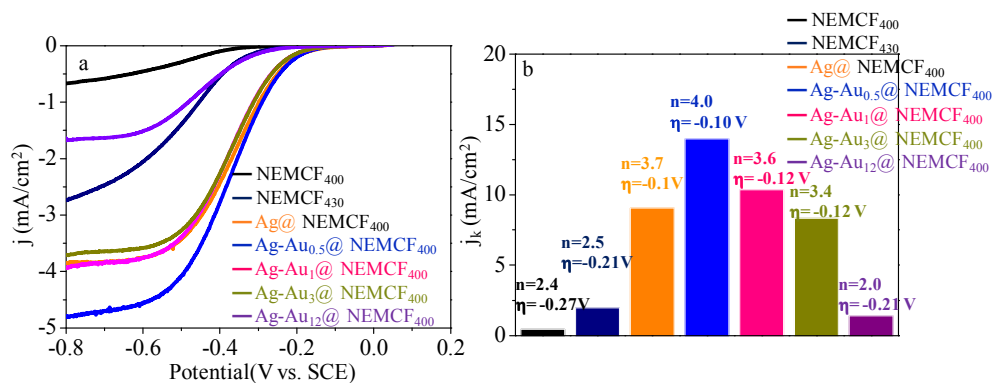


Figure 9 RDE curves of NEMCF₄₀₀ (dark color), NEMCF₄₃₀ (dark blue), Ag@NEMCF₄₀₀ (orange color), Ag-Au_{0.5}@NEMCF₄₀₀ (blue color), Ag-Au₁@NEMCF₄₀₀ (pink color), Ag-Au₃@NEMCF₄₀₀ (green color), and Ag-Au₁₂@NEMCF₄₀₀ (purple color) in O₂-saturated 0.1 M KOH at a scan rate of 10 mVs⁻¹ at 1600 rpm; (b) The electron transfer number and the kinetic limiting current are determined from slopes of K-L plots. The catalysts from left to right were NEMCF₄₀₀, NEMCF₄₃₀, Ag@NEMCF₄₀₀, Ag-Au_{0.5}@NEMCF₄₀₀, Ag-Au₁@NEMCF₄₀₀, Ag-Au₃@NEMCF₄₀₀, and Ag-Au₁₂@NEMCF₄₀₀

The catalytic properties of Ag@NEMCF₄₀₀ and Ag-Au_x@NEMCF₄₀₀ hybrids were first assessed with CV in a KOH solution (0.1 M, saturated with N₂ and O₂) (see Figure S9–S10). Featureless voltammetric currents within the potential range -0.8 to +0.1 V were again present for Ag@NEMCF₄₀₀ and Ag-Au_x@NEMCF₄₀₀ hybrids in the N₂-saturated solution. In contrast, a cathodic peak is discernible for all metal/NEMCF hybrids. Figure 9a shows the RDE curves of Ag-Au_x@NEMCF₄₀₀ hybrids supported on a glassy carbon electrode in O₂-saturated KOH (0.1 M) with scan rate 10 mV s⁻¹ and at speed 1600 rpm of rotation. Figure 9b shows the electron transfer number and current density (j_k) of metal/NEMCF hybrids obtained from the slope and the ordinate intercept of the K–L plots of j^{-1} versus $w^{-1/2}$ at potential -0.5V. The hybrids of NEMCF loaded with Ag and Ag-Au_{0.5} NP greatly enhanced the electrochemical performance, resulting in a four-electron transfer path in the ORR. The Ag-Au_{0.5}@NEMCF₄₀₀ hybrid showed the best catalytic performance with the least

negative onset potential ($\eta = -0.1$ V vs SCE) and with the greatest dynamic limiting current, about 13.97 mA at -0.5 V vs SCE; Ag-Au₁@ NEMCF₄₀₀, Ag-Au₃@ NEMCF₄₀₀ and Ag-Au₁₂@ NEMCF₄₀₀ hybrids, which have increased content of Au, showed depressed catalytic performance of ORR. Even the Ag-Au₁₂@ NEMCF₄₀₀ hybrid showed much worse ORR properties, displaying a more negative onset potential, smaller electron transfer numbers and j_k . The correlation between the increased content of the Au component and the ORR performance requires further interpretation. Previous authors who studied the correlation between ORR and the Au NP size demonstrated that a two-electron path is favored in ORR for NP with size less than 2~3 nm, but a large size of Au NP tends to favor a four-electron path.^{44, 87-88} This interpretation also accounts for the trend of ORR performance observed here. With immersion of Ag@NEMCF in a solution containing Au ions for a short duration, Au first grew as nanoclusters (NC) with a large density of sites with low coordination through slow GRR. The NC were active as the sites of low coordination were more polar and favored further reduction of HO₂⁻ absorption to form OH⁻ absorption via a four-electron path in ORR.^{44, 87-88} Once the NC further grew beyond a certain size to form Au NP, the surface of the Au NP became inactive, resulting in a worse ORR performance with a two-electron path for Ag-Au₁₂@NEMCF₄₀₀.

Conclusions:

Block copolymers with one block containing a nitrogen-rich source of carbon was converted into nitrogen-enriched mesoporous carbon framework nanostructures of pore size 6.3 nm and total surface area 48.3 m²/g when pyrolyzed at 400 °C. The micropores dispersed through the carbon framework provided nanoconfined space for decoration of two size distributions of compact Ag NP with a sharp interface. Because of the nanoscale confinement imparted by the NEMCF matrix, the kinetics of GRR between Ag and Au were retarded. As a result, the surface of Ag NP was attached by gold NC or NP, controlled with GRR for various intervals. At early stages of GRR, Au NC preferentially grew at the expense of Ag NP to develop Ag-Au alloys of which the surface had many defects; the surface of binary metal alloys was hence rough. In contrast, prolonged GRR led to not only the growth of Au NP of large size but also the detachment of binary Ag-Au alloys from the NEMCF matrix. Without the confinement, the dispersion of the detached binary Ag-Au alloys became poor and hence favored aggregation.

We demonstrated also correlations among the electrocatalytic activity of ORR in basic media, nitrogen configurations of NEMCF, and metal particulate dispersion and dimension within the NEMCF matrix. As both pyridinic- and pyrrolic-nitrogen species were present to a greater extent than graphitic-nitrogen species, a two-electron reaction path and sluggish reaction kinetics were found for NEMCF, but the addition of Ag NP significantly facilitated a four-electron electroreduction path and kinetics. With a brief duration of GRR, only Ag-Au alloys containing few Au nanoclusters at the surface and Ag cores in major proportions exhibited the best catalytic performance. Upon prolonged GRR, Au-rich alloys showed much worse ORR properties, which are ascribed to GRR-induced growth of large Au NP and depressed dispersion of binary metal alloys.

Acknowledgements

The authors thank Kuo-Chih Shih and Wei-Cheng Lin for quantitative analysis of GISAXS data. Financial supports from the Ministry of Science and Technology (grant number MOST 104–2221–E–008–125-MY3) and the NCU-ITRI joint R&D research center (grant number FY104-5) are gratefully acknowledged.

†Electronic supplementary information (ESI) available. Figure S1: XPS characterization of NEMCF₄₃₀; Figure S2: ORR performance of NEMCF₄₀₀; Figure S3: AFM images of Ag NPs; Figure S4: AFM image of Ag@NEMCF₄₃₀; Figure S5: TGA and DTG curves of Ag@P2VP; Figure S6: UV-vis absorption of Ag/carbon hybrids; Figure S7: UV-Vis absorption and SEM image of Ag NP and Ag-Au NC; Figure S8: SEM images of Ag@NEMCF₄₀₀, Ag-Au₁@NEMCF₄₀₀ and Ag-Au₁₂@NEMCF₄₀₀; Figure S9-S10: CV and ORR performance of Ag@NEMCF₄₃₀, Ag-Au_{0.5}@NEMCF₄₃₀, Ag-Au₁@NEMCF₄₃₀, Ag-Au₃@NEMCF₄₃₀ and Ag-Au₁₂@NEMCF₄₃₀. See DOI:

Notes and References:

- 1 L. Dai, *Acc. Chem. Res.* 2013, **46**, 31-42.
- 2 M. Liu, R. Zhang, and W. Chen, *Chem. Rev.* 2014, **114**, 5117-5160.
- 3 K. Gong, F. Du, Z. Xia, M. Durstock, and L. Dai, *Science* 2009, **323**, 760-764.
- 4 L. Qu, Y. Liu, J. -B. Baek, and L. Dai, *ACS Nano* 2010, **4**, 1321-1326.
- 5 Y. Li, Y. Zhao, H. Cheng, Y. Hu, G. Shi, L. Dai, and L. Qu, *J. Am. Chem. Soc.* 2012, **134**, 15-18.
- 6 D. Wei, Y. Liu, Y. Wang, H. Zhang, L. Huang, and G. Yu, *Nano Lett.* 2009, **9**, 1752-1758.
- 7 A. L. M. Reddy, A. Srivastava, S. R. Gowda, H. Gullapalli, M. Dubey, and P. M. Ajayan, *ACS Nano* **2010**, **4**, 6337-6342.
- 8 C. H. Zhang, L. Fu, N. Liu, M. H. Liu, Y. Y. Wang, and Z. F. Liu, *Adv. Mater.* 2011, **23**, 1020-1024.
- 9 Y. Wang, Y. Shao, D. W. Matson, J. Li, and Y. Lin, *ACS Nano* 2010, **4**, 1790-1798.
- 10 L. Lai, J. R. Potts, D. Zhan, L. Wang, C. K. Poh, C. Tang, H. Gong, Z. Shen, J. Lin, and R. S. Ruoff, *Energy Environ. Sci.* 2012, **5**, 7936-7942.
- 11 Z. -H. Sheng, L. Shao, J. -J. Chen, W. -J. Bao, F. -B. Wang, and X. -H. Xia, *ACS Nano* 2011, **5**, 4350-4358.
- 12 S. -S. Kim, Y. -R. Kim, T. D. Chung, and B. -H. Sohn, *Adv. Funct. Mater.* 2014, **24**, 2764-2771.
- 13 H. Yin, H. Tang, D. Wang, Y. Gao, and Z. Tang, *ACS Nano* 2012, **6**, 8288-8297.
- 14 R. Zhou, and S. Z. Qiao, *Chem. Mater.* 2014, **26**, 5868-5873.
- 15 G. Goncalves, and P. A. A. P. Marques, C. M. Granadeiro, H. I. S. Nogueira, M. K. Singh, and J. Grácio, *Chem. Mater.* 2009, **21**, 4796-4802.
- 16 J. Shen, M. Shi, N. Li, B. Yan, H. Ma, Y. Hu, and M. Ye, *Nano Res.* 2010, **3**, 339-349.
- 17 K. Vinodgopal, M. Haria, D. Meisel, and P. Kamat, *Nano Lett.* 2004, **4**, 415-418.
- 18 R. Liu, D. Wu, X. Feng, and K. Müllen, *Angew. Chem. Int. Ed.* 2010, **49**, 2565-2569.
- 19 Y. Tang, B. L. Allen, D. R. Kauffman, and A. Star, *J. Am. Chem. Soc.* 2009, **131**, 13200-13201.
- 20 Y. Zhao, Y. Tang, Y. Chen, and A. Star, *ACS Nano* 2012, **6**, 6912-6921.
- 21 S. B. Darling, *Prog. Polym. Sci.* 2007, **32**, 1152-1204.
- 22 J. K. Kim, S. Y. Yang, Y. Lee, and Y. Kim, *Prog. Polym. Sci.* 2010, **35**, 1325-1349.
- 23 S. Valkama, A. Nykanen, H. Kosonen, R. Ramani, F. Tuomisto, P. Engelhardt, G. ten Brinke, O. Ikkala, and J. Ruokolainen, *Adv. Funct. Mater.* 2007, **17**, 183-190.
- 24 C. Liang, K. Hong, G. A. Guiochon, J. W. Mays, and S. Dai, *Angew. Chem. Int. Ed.* 2004, **43**, 5785-5789.

- 25 Y. Wan, Y. Shi, and D. Zhao, *Chem. Mater.* 2008, **20**, 932-945.
- 26 J. Schuster, R. Köhn, M. Döblinger, A. Keilbach, H. Amenitsch, and T. Bein, *J. Am. Chem. Soc.* 2012, **134**, 11136-11145.
- 27 C. Tang, A. Tracz, M. Kruk, R. Zhang, D. M. Smilgies, K. Matyjaszewski, and T. Kowalewski, *J. Am. Chem. Soc.* 2005, **127**, 6918-6919.
- 28 T. Kowalewski, N. V. Tsarevsky, and K. Matyjaszewski, *J. Am. Chem. Soc.* 2002, **124**, 10632-10633.
- 29 J. M. Leiston-Belanger, J. Penelle, and T. P. Russell, *Macromolecules* 2006, **39**, 1766-1770.
- 30 R. M. Ho, T. -C. Wang, C. -C. Lin, T. -L. Yu, *Macromolecules* 2007, **40**, 2814-2821.
- 31 J. Huang, C. Tang, H. Lee, T. Kowalewski, and K. Matyjaszewski, *Macro. Chem. Phys.* 2007, **208**, 2312-2320.
- 32 Y. Wang, J. Liu, S. Christiansen, D. H. Kim, U. Gösele, and M. Steinhart, *Nano Letters* 2008, **8**, 3993-3997.
- 33 D. A. Rider, K. Liu, J. -C. Eloi, L. Vanderark, L. Yang, J. -Y. Wang, D. Grozea, Z. -H. Lu, T. P. Russell, and I. Manners, *ACS Nano* 2008, **2**, 263-270.
- 34 M. Zhong, E. K. Kim, J. P. McGann, S. -E. Chun, J. F. Whitacre, M. Jaroniec, K. Matyjaszewski, and T. Kowalewski, *J. Am. Chem. Soc.* 2012, **134**, 14846-14857.
- 35 M. Zhong, S. Jiang, Y. Tang, E. Gottlieb, E. K. Kim, A. Star, K. Matyjaszewski, and T. Kowalewski, *Chem. Sci.* 2014, **5**, 3315-3319.
- 36 M. Aizawa, and J. M. Buriak, *Chem. Mater.* 2005, **17**, 8932-8933.
- 37 M. Aizawa, and J. M. Buriak, *Chem. Mater.* 2007, **19**, 5090-5101.
- 38 Y. Kim, H. Han, Y. Kim, W. Lee, M. Alexe, S. Baik, and J. K. Kim, *Nano Letters* 2010, **10**, 2141-2146.
- 39 H. G. Boyen, G. Kästle, K. Zürn, T. Herzog, F. Weigl, P. Ziemann, O. Mayer, C. Jerome, M. Möller, J. P. Spatz, M. G. Garnier, P. Oelhafen, *Adv. Funct. Mater.* 2003, **13**, 359-364.
- 40 J. P. Spatz, V. Z. H. Chan, S. Mossmer, F. M. Kamm, A. Plettl, P. Ziemann, and M. Moller, *Adv. Mater.* 2002, **14**, 1827-1832.
- 41 T. Lohmueller, E. Bock, and J. P. Spatz, *Adv. Mater.* 2008, **20**, 2297-2297.
- 42 S. Forster, and M. Antonietti, *Adv. Mater.* 1998, **10**, 195-195.
- 43 W. J. Cho, Y. Kim, and J. K. Kim, *ACS Nano* 2012, **6**, 249-255.
- 44 W. Tang, H. Lin, A. Kleiman-Shwarscstein, G. D. Stucky, and E. W. McFarland, *J. Phys. Chem. C* 2008, **112**, 10515-10519.
- 45 Y. H. Jang, S. T. Kochuveedu, Y. J. Jang, H. -Y. Shin, S. Yoon, M. Steinhart, and D. H. Kim, *Carbon* 2011, **49**, 2120-2126.
- 46 Y. J. Jang, Y. H. Jang, S. -B. Han, D. Khatua, C. Hess, H. Ahn, D. Y. Ryu, K. Shin,

- K. –W. Park, M. Steinhart, and D. H. Kim, *ACS Nano* 2013, **7**, 1573-1582.
- 47 S. Kline, *J. Appl. Crystallogr.* 2006, **39**, 895-900.
- 48 R. J. Roe, *Methods of X-ray and neutron scattering in polymer science* Oxford University Press: New York 2000
- 49 G. Beaucage, *J. Appl. Crystallogr.* 1995, **28**, 717-728.
- 50 S. –H. Wang, Y. –S. Sun, A. S. –T. Chiang, H. –F. Hung, M. –C. Chen, and K. Wood, *J. Phys. Chem. C* 2011, **115**, 11941-11950.
- 51 R. B. Bird, W. E. Stewart and E. N. Lightfoot. *Transport Phenomena; Revised 2nd Ed.*, John Wiley & Sons, Inc. 2007, Chap.6; pp 190.
- 52 D. R. McKenzie, D. Muller, and B. A. Pailthorpe, *Phys. Rev. Lett.* 1991, **67**, 773-776.
- 53 S. Maldonado, S. Morin, and K. J. Stevenson, *Carbon* 2006, **44**, 1429-1437.
- 54 A. Cuesta, P. Dhamelincourt, J. Laureyns, A. Martínez-Alonso, and J. M. D. Tascón, *Carbon* 1994, **32**, 1523-1532.
- 55 F. Bonhomme, J. C. Lassegues, and L. Servant, *J. Electrochem. Soc.* 2001, **148**, E450-E458.
- 56 R. J. Nemanich, and S. A. Solin, *Phys. Rev. B* 1979, **20**, 392-401.
- 57 M. Endo, T. Hayashi, S. –H. Hong, T. Enoki, and M. S. Dresselhaus, *Journal of Applied Physics* 2001, **90**, 5670-5674.
- 58 M. M. Browne, G. V. Lubarsky, M. R. Davidson, and R. H. Bradley, *Surf. Sci.* 2004, **553**, 155-167.
- 59 D. O. H. Teare, N. Emmison, C. Ton-That, and R. H. Bradley, *Langmuir* 2000, **16**, 2818-2824.
- 60 C. Ton-That, D. O. H. Teare, P. A. Campbell, and R. H. Bradley, *Surf. Sci.* 1999, **433–435**, 278-282.
- 61 K. Stańczyk, R. Dziembaj, Z. Piwowarska, and S. Witkowski, *Carbon* 1995, **33**, 1383-1392.
- 62 J. R. Pels, F. Kapteijn, J. A. Moulijn, Q. Zhu, and K. M. Thomas, *Carbon* 1995, **33**, 1641-1653.
- 63 A. J. Bard, and L. R. Faulkner Wiley Electrochemical methods. Fundamentals and applications: New York 2001.
- 64 Y. Li, W. Zhou, H. Wang, L. Xie, Y. Liang, F. Wei, J. –C. Idrobo, S. J. Pennycook, and H. Dai, *Nat Nano* 2012, **7**, 394-400.
- 65 L. Yu, X. Pan, X. Cao, P. Hu, and X. Bao, *J. Catal.* 2011, **282**, 183-190.
- 66 S. Yang, X. Feng, X. Wang, and K. Müllen, *Angew. Chem., Int. Ed.* 2011, **50**, 5339-5343.
- 67 S. –A. Wohlgemuth, T. –P. Fellingner, P. Jaker, and M. Antonietti, *J. Mater. Chem. A* 2013, **1**, 4002-4009.

- 68 D. Geng, Y. Chen, Y. Chen, Y. Li, R. Li, X. Sun, S. Ye, and S Knights, *Energy Environ. Sci.* 2011, **4**, 760-764.
- 69 Q. Li, S. Zhang, L. Dai, and L. -S. Li, *J. Am. Chem. Soc.* 2012, **134**, 18932-18935.
- 70 T. Xing, Y. Zheng, L. H. Li, B. C. C. Cowie, D. Gunzelmann, S. Z. Qiao, S. Huang, and Y. Chen, *ACS Nano* 2014, **8**, 6856-6862.
- 71 K. E. Lee, J. E. Kim, U. N. Maiti, J. Lim, J. O. Hwang, J. Shim, J. J. Oh, T. Yun, and S. O. Kim, *ACS Nano* 2014, **8**, 9073-9080.
- 72 C. -T. Hung, N. Yu, C. -T. Chen, P. -H. Wu, X. Han, Y. -S. Kao, T. -C Liu, Y. Chu, F. Deng, A. Zheng, and S. -B. Liu, *J. Mater. Chem. A.* 2014, **2**, 20030-20037.
- 73 L. Zhang, and Z. Xia, *J. Phys. Chem. C.* 2011, **115**, 11170-11176.
- 74 X. Bao, X. Nie, D. von Deak, E. Biddinger, W. Luo, A. Asthagiri, U. Ozkan, and C. Hadad, *Top Catal* 2013, **56**, 1623-1633.
- 75 Z. Luo, S. Lim, Z. Tian, J. Shang, L. Lai, B. MacDonald, C. Fu, Z. Shen, T. Yu, and J. Lin, *J. Mater. Chem.* 2011, **21**, 8038-8044.
- 76 F. L. Yap, P. Thoniyot, S. Krishnan, and S. Krishnamoorthy, *ACS Nano* 2012, **6**, 2056-2070.
- 77 S. Moussa, G. Atkinson, M. SamyEl-Shall, A. Shehata, K. M. AbouZeid, and M. B. Mohamed, *J. Mater. Chem.* 2011, **21**, 9608-9619.
- 78 L. Jensen, C. M. Aikens, and G. C. Schatz, *Chem. Soc. Rev.* 2008, **37**, 1061-1073.
- 79 A. M. Goodman, Y. Cao, C. Urban, O. Neumann, C. Ayala-Orozco, M. W. Knight, A. Joshi, P. Nordlander, and N. J Halas, *ACS Nano* 2014, **8**, 3222-3231.
- 80 S. Preciado-Flores, D. Wang, D. A. Wheeler, R. Newhouse, J. K. Hensel, A. Schwartzberg, L. Wang, J. Zhu, M. Barboza-Flores, and J. Z. Zhang, *J. Mater. Chem.* 2011, **21**, 2344-2350.
- 81 A. M. Schwartzberg, T. Y. Olson, C. E. Talley, and J. Z. Zhang, *J. Phys. Chem. B.* 2006, **110**, 19935-19944.
- 82 Y. Sun, Z. Tao, J. Chen, T. Herricks, Y. Xia, *Am. Chem. Soc.* 2004, **126**, 5940-5941.
- 83 V. Vongsavat, B. M. Vittur, W. W. Bryan, J. -H. Kim, and T. R. Lee, *ACS Appl. Mater. Interfaces* 2011, **3**, 3616-3624.
- 84 K. Zhang, T. Holloway, A. Wingfield, J. Pradhan, W. K. Cao, and A. Pradhan, *Micro Nanosyst.* 2011, **3**, 76;
- 85 Y. Sun, B. T. Mayers, and Y. Xia, *Nano Lett.* 2002, **2**, 481-485.
- 86 W. Wang, M. Dahl, and Y. Yin, *Chem. Mater.* 2013, **25**, 1179-1189.
- 87 W. Chen, and S. Chen, *Angew. Chem. Int. Ed.* 2009, **48**, 4386-4389.
- 88 C. Jeyabharathi, S. Senthil Kumar, G. V. M. Kiruthika, and K. L. N. Phani, *Angew. Chem. Int. Ed.* 2010, **49**, 2925-2928.

Table of Contents

Electrocatalytic Activity of Nitrogen-rich Mesoporous Carbon Framework and its Hybrids with Metal Nanoparticles Fabricated through Pyrolysis of Block CopolymersYen-Hsing Lu, Jiun-You Liou, Chien-Fu Lin, and Ya-Sen Sun^{a*}